



## Full Length Article

## Fluence profiling at JSI TRIGA reactor irradiation facility

V. Sola <sup>a,b,\*</sup>, I. Mandić <sup>c</sup>, K. Ambrožič <sup>c</sup>, O.A. Marti Villarreal <sup>a,b,1</sup>, M. Ferrero <sup>b</sup>, G. Kramberger <sup>c</sup>, L. Snoj <sup>c</sup>

<sup>a</sup> Università degli Studi di Torino, via P. Giuria 1, 10125, Torino, Italy

<sup>b</sup> INFN, Sezione di Torino, via P. Giuria 1, 10125, Torino, Italy

<sup>c</sup> Institut Jožef Stefan, Jamova cesta 39, 1000 Ljubljana, Slovenia

## ARTICLE INFO

## Keywords:

TRIGA reactor

LGAD

Irradiation facility

Fluence profile

## ABSTRACT

We present an analysis of the fluence profile at the JSI TRIGA neutron reactor facility in Ljubljana. For the study, multi-pad Low-Gain Avalanche Diodes (LGADs) are used. The deactivation of acceptor doping in the gain layer implant due to the irradiation, typical of LGAD devices, is exploited to map the fluence profile inside the irradiation channels. The amount of active doping of the LGAD gain layer is extracted via capacitance–voltage measurements for each pad before and after irradiation to a fluence of  $1.5 \times 10^{15} n_{eq}/\text{cm}^2$ , where  $n_{eq}$  stands for 1 MeV equivalent neutron count, providing a precise and prompt measurement of the fluence distribution over the LGAD sensor. Experimental results are compared to neutron fluence expectations calculated with Monte Carlo techniques.

## 1. Introduction

The TRIGA Mark II reactor at the Jožef Stefan Institut (JSI) [1] is extensively used by the High Energy Physics community to study and test radiation damage effects on detector materials and read-out electronics [2].

Recently, the increasing sensitivity of silicon devices to the effects of radiation triggered the discussion on the fluence spread that can affect irradiation campaigns. In particular, performance variation of Low-Gain Avalanche Diodes (LGADs) after irradiation [3] suggested the possibility to precisely map the fluence profile at the JSI facility.

LGADs are n-in-p silicon sensors with a highly p-doped region close to the n-electrode, called gain implant, to create a local enhancement of the electric field responsible for the charge carrier multiplication [4]. It has been observed that the Boron dopants in the gain layer get deactivated by the radiation. This effect is known as acceptor removal [5] and has been precisely characterised and tested [6], opening the possibility to use LGADs as devices suitable to measure the fluence variation inside the irradiation channels of the JSI facility.

LGAD sensors have been used with a straightforward procedure and have proven to be an effective tool to build a fluence profile map inside the reactor core.

## 2. The experimental method

The idea behind the present measurement is to use LGAD arrays of pixels to precisely quantify the different neutron fluence experienced by each pixel. For this purpose, sensors from wafer 1 of the FBK USFD3 production batch [7] have been used, made of an array of  $5 \times 5$  pixels. A drawing of the sensors is shown in Fig. 1: the area of each pixel is  $1.3 \text{ mm} \times 1.3 \text{ mm}$ , and the total sensor area is  $7.7 \text{ mm} \times 7.7 \text{ mm}$ .

The study exploits the deactivation of the gain implant dopants by particle radiation known as acceptor removal and parametrised as

$$N_A(\Phi) = N_A(0) \cdot e^{-c\Phi} \quad (1)$$

where  $N_A(0)$  ( $N_A(\Phi)$ ) is the effective acceptor density of the gain layer before irradiation (after a fluence  $\Phi$ ), and  $c$  is the removal coefficient, depending on the initial doping and on the gain layer design. The  $c$  coefficient has been extensively measured through several campaigns [6,8].

The determination of the active acceptor concentration is performed through capacitance–voltage (C–V) measurements. The value of the bias voltage at which the gain layer is depleted corresponds to a drop in the measured capacitance, defined as a knee (see Fig. 2) and indicated as  $V_{GL}$ .

In particular, for each pad, the  $V_{GL}$  has been defined as the point at which the capacitance reaches a fixed value in the proximity of

\* Corresponding author at: Università degli Studi di Torino, via P. Giuria 1, 10125, Torino, Italy.

E-mail address: [valentina.sola@cern.ch](mailto:valentina.sola@cern.ch) (V. Sola).

URL: <http://l.infn.it/vsola/> (V. Sola).

<sup>1</sup> Now at Fondazione Bruno Kessler, via Sommarive 18, 38123, Povo, Italy.

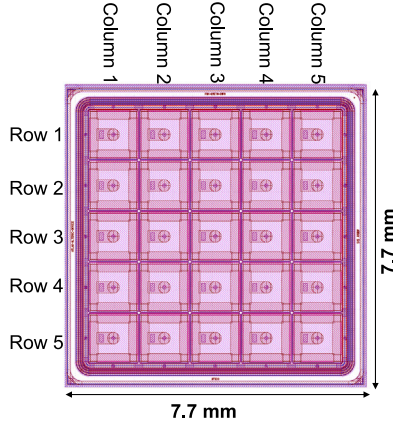


Fig. 1. Schematic draw of the FBK sensors used for the study.

the knee, assuming that for a fixed pad geometry, an equal value of capacitance represents the identical amount of depleted volume, making the measurement extremely sensitive to the changes in active doping. Such capacitance value has been chosen to be 150 pF for both un-irradiated and irradiated sensors. It is worth noting that the method has been proven to be equivalent to other methods used to extract  $V_{GL}$ , e.g. in [6]. Furthermore, it guarantees a prompt and easy tool to access a precise estimate of the active doping at a given depth inside the pad under test.

To eliminate the effects of non-uniformities of gain layer doping implantation and systematic uncertainties on the gain layer depletion measurement, the ratio of  $V_{GL}$  before and after irradiation will be considered. Therefore, from the variation of

$$\frac{V_{GL}(\Phi)}{V_{GL}(0)} = e^{-c\Phi}, \quad (2)$$

and assuming a constant  $c$ , which is a valid assumption considering an initial doping variation of less than 2% [9], the measured variation of the ratio directly quantifies a variation in the received fluence.

For the present study, 8 LGAD sensors have been irradiated to a fluence of  $1.5 \times 10^{15} \text{ n}_{\text{eq}}/\text{cm}^2$  by using the channel F19 of the JSI reactor [10]. This channel is the one mainly used to irradiate samples for high-energy physics detector developments. The irradiation has been done at full reactor power of 250 kW. At such power, the target fluence in channel F19 is reached in 926 s.

### 3. The experimental setup

For irradiation at the JSI facility, cylindrical plastic containers with a diameter of about 2 cm and a height of about 10 cm are used. By placing the LGAD sensors in a fixed position inside a container, it is possible to investigate and map the geometrical variation of the neutron flux inside the irradiation volume.

Eight sensors have been fixed on plastic support and placed at two different depths inside the container. The support consists of four arms placed orthogonally to each other, and four sensors have been attached at the same depth on each arm of the plastic strut, as shown in Fig. 3.

The pad-by-pad C-V characterisation before and after irradiation has been performed at room temperature, connecting a Keysight B1505A Power Device Analyzer to the probe station. A high voltage source-monitor unit was used together with a multi-frequency capacitance measurement unit, interfaced via a bias-T and referred to a common ground value. The frequency of the AC signal was set to 1 kHz, with an amplitude of 50 mV, and a parallel capacitor-resistor model was used to extract the capacitance value. The chuck of the probe station was negatively biased, and one needle at zero voltage moved over the 25 pads of each sensor. One additional needle set at zero voltage has

been used to ground the guard ring of the sensor in order to collect dark current from the sensor periphery and reduce the noise on the capacitance measurement.

### 4. The measurement technique

For all the  $1.3 \text{ mm} \times 1.3 \text{ mm}$  measured pads,  $V_{GL}$  has been extracted as the voltage value at which the capacitance reaches 150 pF. As the reverse voltage was provided to the sensor in steps of 0.2 V, to estimate the gain layer depletion voltage, a linear fit to the two capacitance measurements immediately lower ( $C_{\text{low}}$ ) and higher ( $C_{\text{high}}$ ) than 150 pF has been performed, according to

$$V_{GL} = V_{\text{low}} + \frac{V_{\text{high}} - V_{\text{low}}}{C_{\text{high}} - C_{\text{low}}} \cdot (150 \text{ pF} - C_{\text{low}}), \quad (3)$$

being  $V_{\text{low}}$  and  $V_{\text{high}}$  the measured voltage values preceding and following the  $V_{GL}$  point, respectively. The linear fit represents a good approximation of the evolution of the C-V characteristics, given the small interval used in the voltage measurement.

The  $V_{GL}$  values extracted for the sensor 16-6 before and after irradiation to a fluence of  $1.3 \times 10^{15} \text{ n}_{\text{eq}}/\text{cm}^2$  are shown in Fig. 4. Prior to irradiation, it is possible to observe the non-uniformity in the dopant implantation on the gain layer; for the sensor under test, the spread in concentration is measured to be <0.9%. After the irradiation, a modification in the geometrical trend of  $V_{GL}$  non-uniformity become visible, with an increase of its relative spread to about 2%.

As explained in Section 2, for our analysis we will consider the ratio of  $V_{GL}$  before and after irradiation, to remove the effect of initial doping non-uniformities and the sistematics affecting the measurement technique. Fig. 5 shows the resulting ratio for the sensor 16-6: it is possible to observe as irradiation introduces a strong horizontal non-uniformity, while there is no obvious trend as a function of the vertical direction.

As a systematic check, results have been reproduced considering fixed capacitance values of 160 pF and 140 pF. The resulting values of  $V_{GL}$  ratios before and after irradiation are modified by less than 0.1% in the first case, while a maximum spread of -1.2% to 0.6% has been observed in the latter case. This difference might be explained by the fact that for  $C = 140 \text{ pF}$  in irradiated sensors, the curve approaches a kink in the measurement, see Fig. 2 (right): such kink can be due to the reach of a not optimised frequency value used in the measurement process when the depleted volume as a function of the applied bias moves from the gain implant to the sensor bulk region. Therefore, a systematic uncertainty of 0.9% is attributed to all the measured values of the  $V_{GL}$  ratio.

Also, the results of the fixed capacitance method have been compared with the method that considers the cusp in the parallel resistance as a function of the bias ( $V_{GL}^R$  in [6]). The difference in the results between the two methods has been measured to be of 1.4%. However, it is important to note that the  $V_{GL}^R$  method guarantees a minor precision at the fluence under test, as at relatively high fluences, the cusp enlarges, resulting in higher uncertainty in determining the exact position of its maximum. Thus, the method of the fixed capacitance provides a more precise estimate of  $V_{GL}$  and the relative difference between the two methods is not considered as an uncertainty of the presented results. .

### 5. The simulation

The experiment was reproduced by Monte Carlo particle transport simulations using the MCNP v.6.1 [11] code with ENDF/B-VII.0 nuclear data libraries [12]. Computations were performed in criticality mode, and results were normalised to full reactor power (250 kW) [13].

A detailed JSI TRIGA reactor model was used, with core configuration and control rod positions resembling the configuration used during the experiment, displayed in Fig. 6 (right). Initial simulations were performed without the sensor assembly in the F19 irradiating

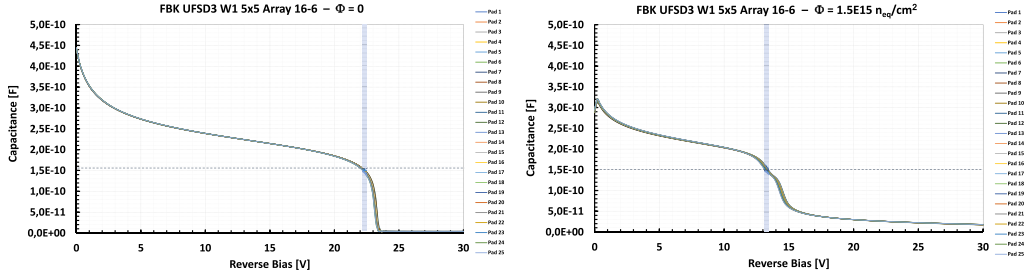


Fig. 2. The C-V characteristics from all the 25 pads of the 16-6 sensor before (left) and after irradiation to a fluence of  $1.5 \times 10^{15} \text{ n}_{\text{eq}}/\text{cm}^2$  (right). The horizontal dotted lines correspond to the value of  $C = 150 \text{ pF}$ , and the vertical bands highlight the corresponding values of reverse bias. The capacitance of full depletion of the pads under test is  $C_{FD} \sim 3.2 \text{ pF}$ .

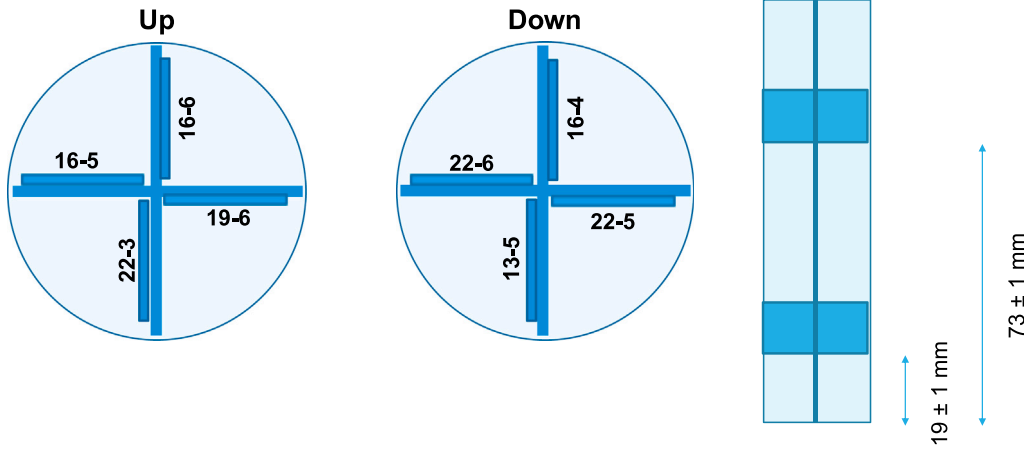


Fig. 3. The placement of the 8 LGAD sensors inside the irradiation container is shown: 4 sensors are placed at two different depths, fixed on a plastic support. The sensor numbering and distance from the container bottom are reported.

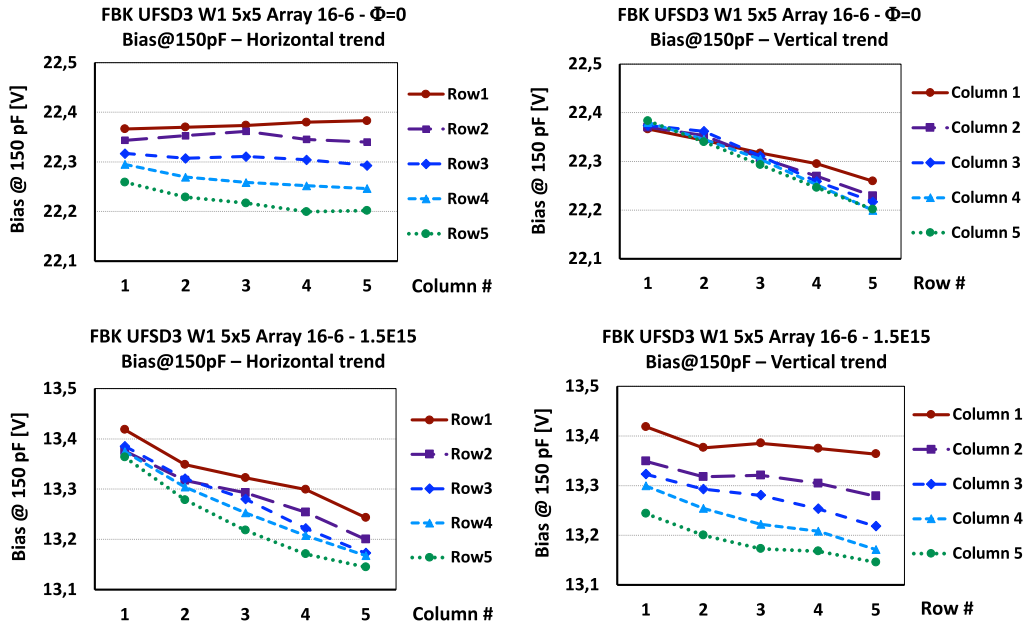


Fig. 4. The extracted values of  $V_{GL}$  for the sensor 16-6 before (top) and after (bottom) irradiation to a fluence of  $1.5 \times 10^{15} \text{ n}_{\text{eq}}/\text{cm}^2$ , reported as a function of the column number (left) and of the row number (right). The distance between the centre of the neighbouring pads and, therefore, the distance between each measured point is 1.3 mm.

channel in order to assess the homogeneity and possible gradients of the fast neutron flux component (neutrons with energy  $E_n > 100 \text{ keV}$ ) within the irradiation position. The neutron flux was calculated on a mesh superimposed over F19 irradiation position with resolution of  $2 \text{ mm} \times 2 \text{ mm} \times 2 \text{ mm}$ . Neutron and gamma fluxes were tallied in three

distinct energy groups, as denoted in Table 1. The fast neutron flux distribution and its gradients in the  $x$  and  $y$  directions are displayed in Fig. 7. One can observe the increase of the fast neutron flux component in close proximity to the neighbouring fuel elements.

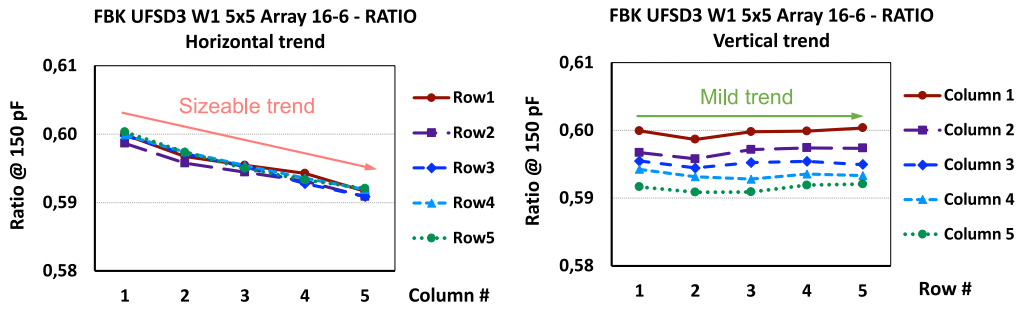


Fig. 5. The ratio of the  $V_{GL}$  values before and after irradiation for the sensor 16-6 is reported as a function of the column number (left) and the row number (right). The distance between the centre of the neighbouring pads and, therefore, the distance between each measured point is 1.3 mm.

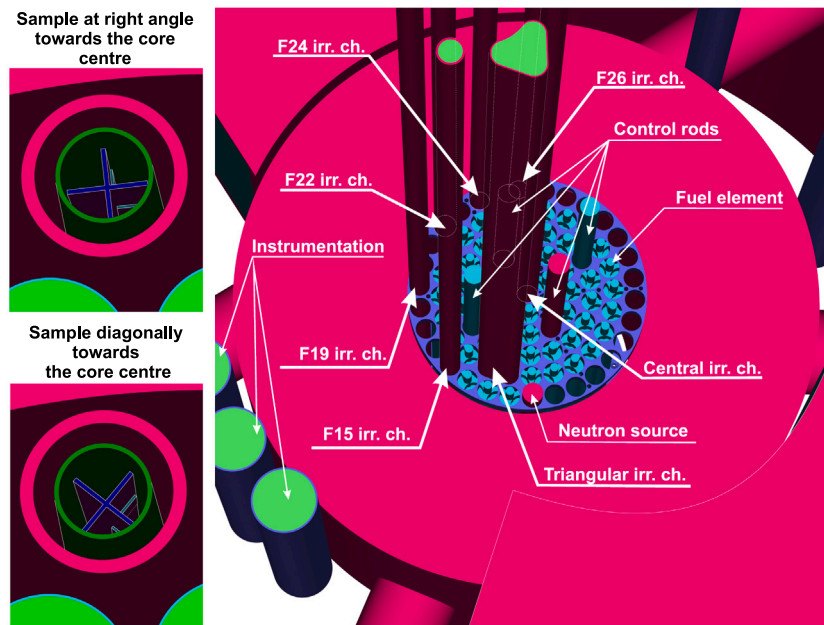


Fig. 6. Two distinct orientations of the sensors inside the irradiation channel (left) and a detailed view of the JSI TRIGA MCNP computational model (right).

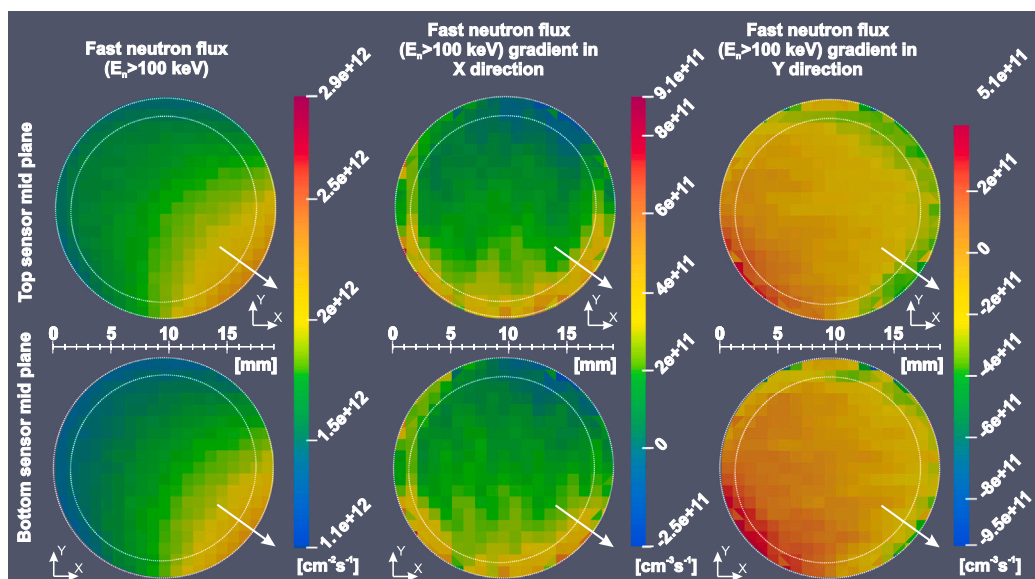


Fig. 7. Fast neutron ( $E_n > 100 \text{ keV}$ ) flux distribution in X-Y direction and their gradients in X and Y direction inside the F19 irradiation channel, at Z-levels corresponding to the mid-depth levels of the inserted sensor assembly. The white dotted line denotes the irradiation channel aluminium walls, while the arrow points to the core centre.

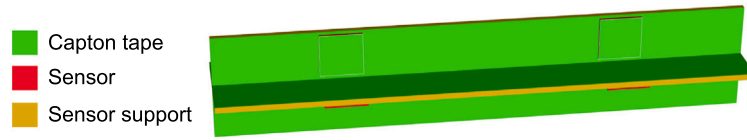


Fig. 8. The model of the LGAD sensor's assembly on FR4 supports, covered with Kapton tape.

Table 1

Lower and upper energy (E) bounds of tallied neutrons and gamma rays.

	Neutron		Gamma	
	Lower E	Upper E	Lower E	Upper E
1	0 eV	0.625 eV	0 eV	100 keV
2	0.625 eV	100 keV	100 keV	1 MeV
3	100 keV	100 MeV	1 MeV	100 MeV

Table 2

Fast neutron flux ( $E_n > 100$  keV) at reactor power of 250 kW. Mean values per sensor and the variation over individual pixels. Mean value of the statistical uncertainty spans from 0.62% to 0.82%, while statistical uncertainties on the mesh span from 2.2% to 2.7%.

No.	Diagonal		Perpendicular	
	Mean [ $\text{cm}^{-2} \text{s}^{-1}$ ]	Variation [%]	Mean [ $\text{cm}^{-2} \text{s}^{-1}$ ]	Variation [%]
1	$1.684 \times 10^{12}$	+5.1 -4.8	$1.510 \times 10^{12}$	+7.3 -6.8
2	$1.741 \times 10^{12}$	+5.5 -4.7	$1.577 \times 10^{12}$	+4.2 -5.1
3	$1.741 \times 10^{12}$	+5.4 -4.2	$1.596 \times 10^{12}$	+4.0 -5.1
4	$1.773 \times 10^{12}$	+4.8 -4.0	$1.633 \times 10^{12}$	+4.7 -3.5
5	$1.556 \times 10^{12}$	+6.1 -6.2	$1.742 \times 10^{12}$	+5.6 -10.2
6	$1.647 \times 10^{12}$	+5.8 -5.6	$1.787 \times 10^{12}$	+6.1 -6.1
7	$1.531 \times 10^{12}$	+6.4 -6.1	$1.648 \times 10^{12}$	+2.7 -2.3
8	$1.607 \times 10^{12}$	+6.9 -5.9	$1.698 \times 10^{12}$	+4.8 -3.5

In the second stage, sensors and the carrier board constituting a cross configuration (see Fig. 3), as well as the polyethylene container, were also modelled in detail and inserted into the irradiation channel into the F19 position, shown in Fig. 6 (right). The sensor support was modelled as the FR4 base plate of 1 mm thickness, while the sensors themselves were modelled as boxes of pure silicon with a size of  $7.7 \text{ mm} \times 7.7 \text{ mm} \times 0.63 \text{ mm}$ . Kapton tape with a thickness of 0.05 mm covering the entire assembly was also modelled. The sensor assembly model is schematically displayed in Fig. 8. The isotopic composition of the above-mentioned materials was obtained using the MATSSF code [14] and is reported in Appendix. Due to the unknown axial orientation during the experiment, two distinct orientations were modelled: with the carrier board cross arms perpendicular to the reactor core centre and with arms diagonal with respect to the core centre, Fig. 6 (left). The same energy group structure was used for tallying neutron and gamma flux in each individual LGAD sensor, as well as on a mesh superimposed over the entire irradiated container with a resolution of  $2 \text{ mm} \times 2 \text{ mm} \times 2 \text{ mm}$ , displayed in Fig. 9, along with numbering of LGAD sensor used in the simulations. The fast neutron flux difference between the empty irradiation channel and with inserted polyethylene container and sensor sample is displayed in Fig. 10. By comparing with simulated flux values shown in Fig. 7, it is possible to appreciate that the insertion of samples changes the neutron flux of the empty irradiation channel by up to  $\sim 10\%$ . Fast neutron flux ( $E_n > 100$  keV) averaged over individual sensor are provided in Table 2. Moreover, each sensor was divided into  $(5 \times 5)$  sections, corresponding to positions of individual pixels (Fig. 1) in order to assess the fast neutron flux variation, sensed by each sensor.

## 6. The results

The ratios of the  $V_{GL}$  before and after irradiation are shown for each pixel as a function of the column number for the eight sensors

Table 3

Average, minimum and maximum fluence ( $\Phi$ ) experienced by each of the eight measured sensors. Fluence values are expressed in units of  $10^{15} \text{ n}_{\text{eq}}/\text{cm}^2$ . Relative variations of the fluences measured by each sensor with respect to the average fluence of  $1.37 \times 10^{15} \text{ n}_{\text{eq}}/\text{cm}^2$  is reported.

Sensor No.	Average $\Phi$	$\Phi$ Min	$\Phi$ Max	Variation [%]
19-6	1.22	1.18	1.26	- 11.2 <sup>-8.6</sup> <sub>-13.8</sub>
22-3	1.35	1.30	1.38	- 1.7 <sup>+0.8</sup> <sub>-5.3</sub>
16-5	1.50	1.46	1.53	+ 9.1 <sup>+11.3</sup> <sub>+6.6</sub>
16-6	1.35	1.33	1.37	- 1.9 <sup>-0.4</sup> <sub>-3.5</sub>
22-5	1.21	1.17	1.23	- 12.1 <sup>+10.1</sup> <sub>-14.7</sub>
13-5	1.40	1.36	1.43	+ 1.9 <sup>+4.2</sup> <sub>-0.8</sub>
22-6	1.55	1.52	1.58	+ 13.1 <sup>+15.4</sup> <sub>+10.7</sub>
16-4	1.41	1.37	1.44	+ 2.7 <sup>+4.6</sup> <sub>-0.1</sub>

under test, split between the top (Fig. 11) and the bottom (Fig. 12) part of the container. For both the top and the bottom positioning, there is one sensor with a high value of the  $V_{GL}$  ratio, above 0.62 (19-6 and 22-5, respectively), one with a low ratio value, below 0.56 (namely, 16-5 and 22-6), and there are two sensors with a medium ratio, of about 0.58 (22-3 and 16-6 in the top part, 13-5 and 16-4 in the bottom part). The orientation of the container during the irradiation inside the F19 channel is unknown. Still, the observed trend in the received fluence is compatible with the gradients shown by the simulation relative to the sensors oriented perpendicularly to the centre of the reactor core, as in Fig. 9 (right). The results suggest that, during the irradiation, the sensors 19-6 and 22-5 were closer to the reactor core centre, while sensors 16-5 and 22-6 were farther away. Moreover, column 1 of each sensor points to the centre of the cross support. Therefore, the opposite trend of the ratios for, e.g., sensors 22-5 and 22-6 indicate that in 22-5, the pixels in column 5 are more exposed to irradiation, while for 22-6, pixels in column 1 experienced higher irradiation, in agreement with the geometrical construction of the setup.

Furthermore, it has been measured that the vertical spread of the fluence is mild, as it is visible from two sensors placed on the same arm of the holder structure, namely, 22-5 in the bottom part and 19-6 in the top one, as shown in Fig. 13. A linear interpolation of the measured  $V_{GL}$  ratios on all the pixels from the column 1 of the sensors 22-5 and 19-6 is displayed: the variation of the ratio values spanning over a vertical distance of 59.2 mm is quantified by the angular coefficient as a parameter of the fit, measured to be  $5.05 \times 10^{-5} \text{ mm}^{-1}$ . Also, the relative difference between the lowest row of the sensor 22-5 (row 5) and the highest row of the sensor 19-6 (row 1) is 0.8% for column 1 and rises to 1.1% in column 5. This observation agrees with the simulation, as in Figs. 9 and 10.

The conversion between the measured ratios of  $V_{GL}$ , reflecting the fraction of active gain implant that survived the irradiation as presented in Eq. (1), to the value of fluence experienced by each pixel make use of the formula in Eq. (2) and uses as value for the acceptor removal coefficient  $c = 3.85 \times 10^{-16} \text{ cm}^2$ , extracted from previous measurements on sensors from the same production batch [15]. The uncertainty on the  $c$  factor is 12% and accounts for the different methods used to extract  $V_{GL}$  at various fluences and from the uncertainty on those fluences, which represent the highest contribution to the uncertainty.

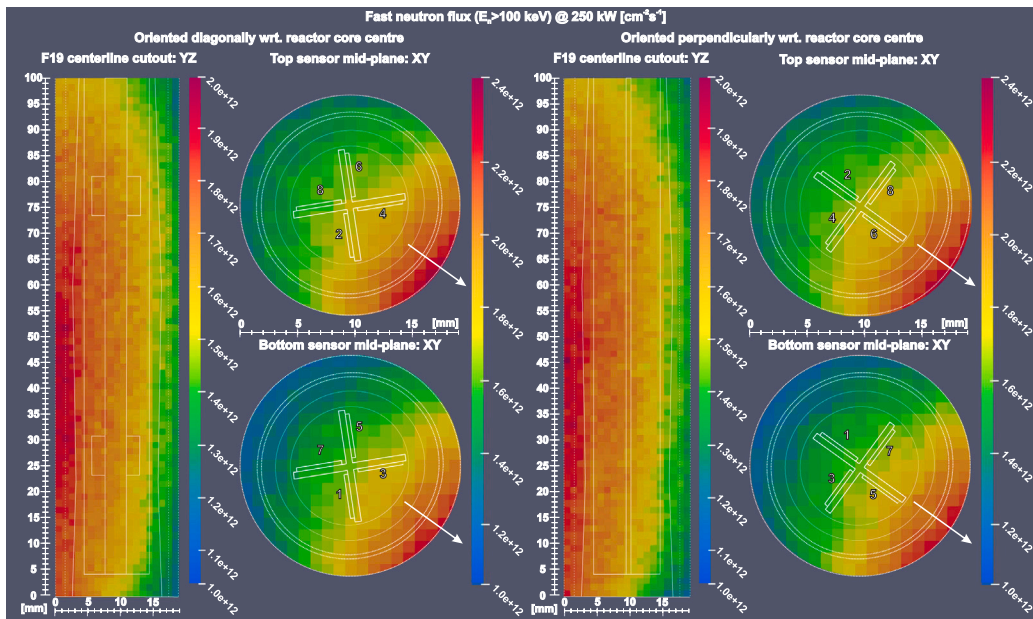


Fig. 9. Fast neutron ( $E_n > 100$  keV) flux field in irradiation position F19 at full reactor power (250 kW) for two sample orientations. Visualisations at the  $z$ -axis and sensor mid-planes. Relative statistical uncertainty  $< 1\%$ . Numbers denote the sensor numbering convention used in calculations, and the arrow indicates the direction towards the reactor core centre. White lines denote the edge of the irradiation channel (dashed), polyethylene container and the PCB with the sensors.

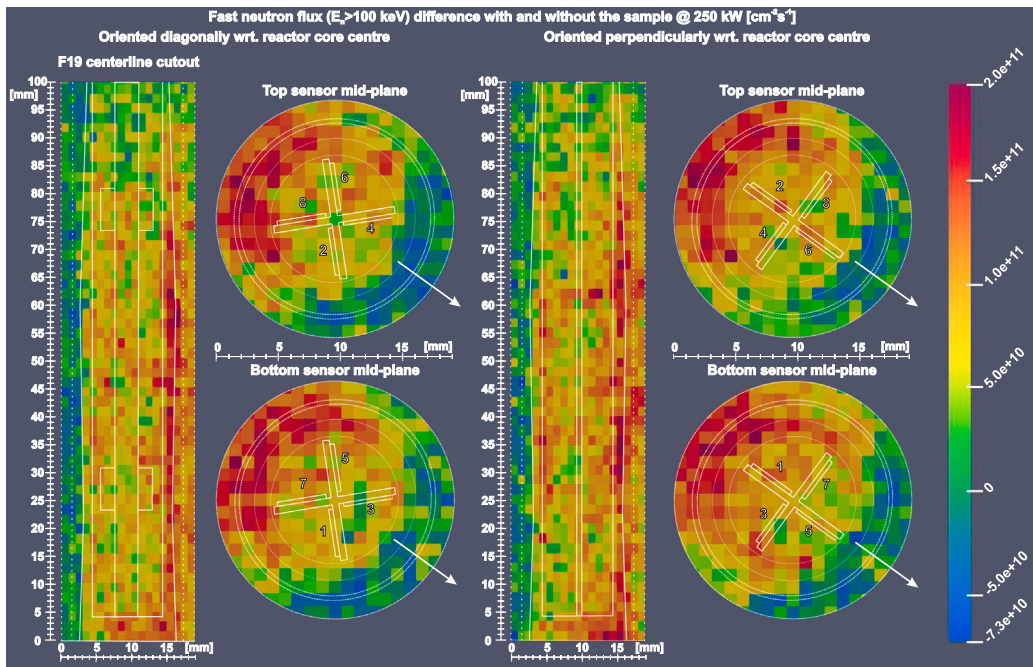


Fig. 10. Fast neutron ( $E_n > 100$  keV) flux field difference in irradiation position F19 at full reactor power (250 kW) between empty irradiation channel and with inserted polyethylene container and sample at two orientations. Visualisations at the  $z$ -axis and sensor mid-planes. Relative statistical uncertainty between 10% to 30%. Numbers denote the sensor numbering convention used in calculations, and the arrow indicates the direction towards the reactor core centre. Lines in the figure denote the edge of the irradiation channel (dashed), polyethylene container and the PCB with the sensors.

Fig. 14 reports the fluence experienced by each tested sensor, averaged over all 25 pixels. The evolution of Eq. (2) for the FBK wafer from which the tested sensors are taken (W1 UFSD3) is superimposed to the data points to highlight the evolution of the  $V_{GL}$  ratio with the fluence. The average fluence experienced by all the  $8 \times 25$  measured pixels is  $\Phi_{ave} = 1.37 \times 10^{15} \text{ n}_{eq}/\text{cm}^2$ ,  $0.13 \times 10^{15} \text{ n}_{eq}/\text{cm}^2$  lower than the expected value of  $1.5 \times 10^{15} \text{ n}_{eq}/\text{cm}^2$ .

The average fluences seen by each sensor are reported in Table 3, together with the minimum and maximum fluence experienced by the

pixels in each of the eight measured sensors. The relative variations are also reported, obtained by comparing the average sensor values with the overall average value equal to  $1.37 \times 10^{15} \text{ n}_{eq}/\text{cm}^2$ . Considering minimum and maximum values of fluence experienced by the pixel, the fluence variation ranges from  $-14.7\%$  to  $15.4\%$ , observed on the sensors placed on the bottom part of the container. The variation in the top region spans between  $-13.7\%$  to  $11.4\%$ .

Concerning the vertical variation of the fluence, it has been observed a minimum difference of  $2.13 \times 10^{13} \text{ n}_{eq}/\text{cm}^2$  between sensors

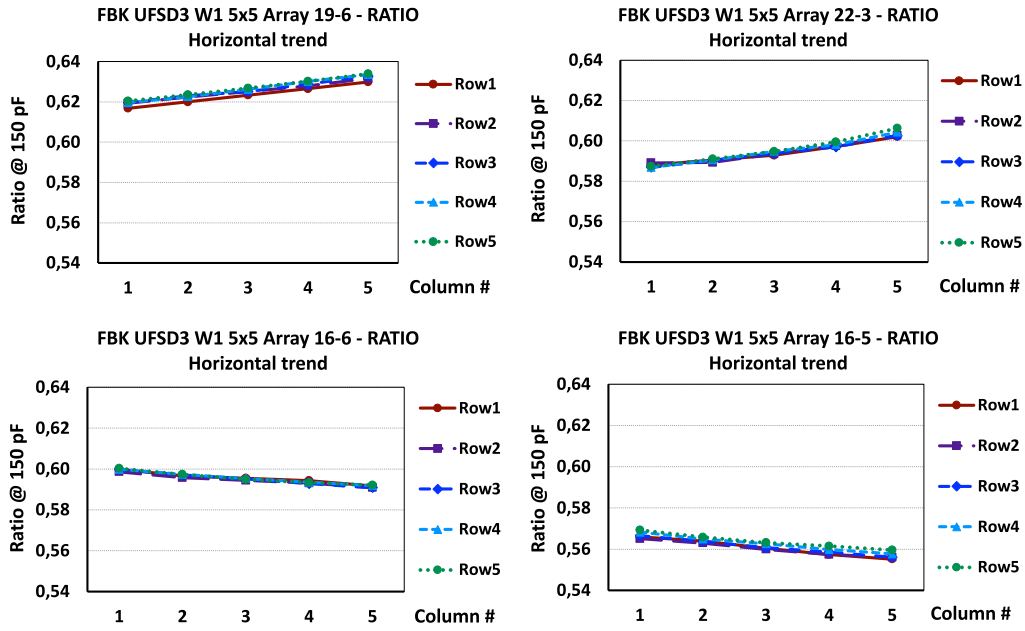


Fig. 11. The ratio of the  $V_{GL}$  values before and after irradiation for the four sensors placed in the top part of the canister. The distance between each measured point is 1.3 mm.

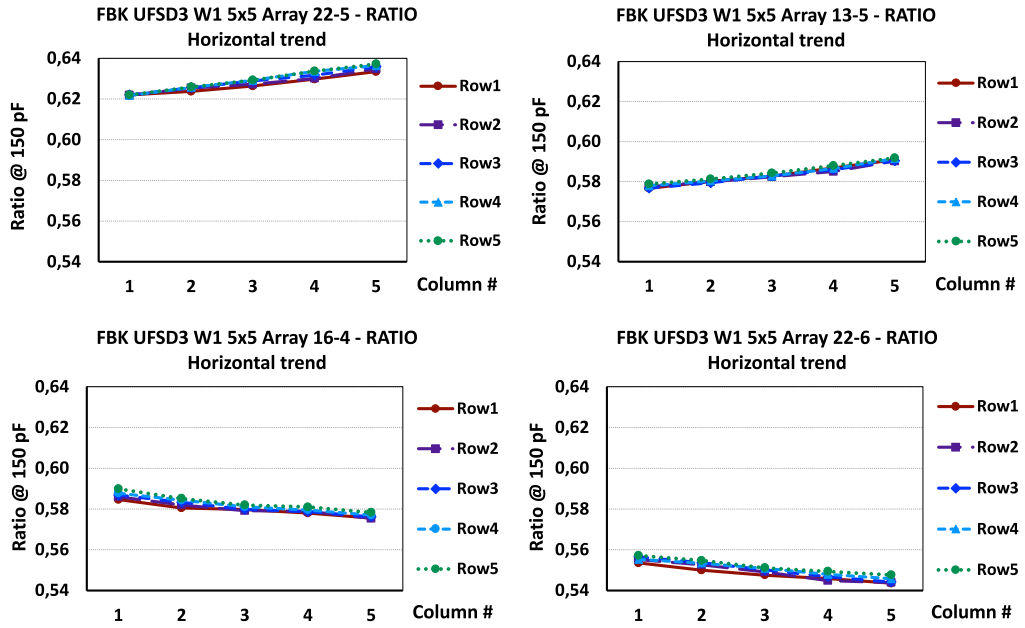


Fig. 12. The ratio of the  $V_{GL}$  values before and after irradiation for the four sensors placed in the bottom part of the canister. The distance between each measured point is 1.3 mm.

19-6 and 22-5 and a maximum difference of  $7.81 \times 10^{13} \text{ n}_{eq}/\text{cm}^2$  between sensors 16-5 and 22-6.

Figs. 15 and 16 compare the results from the data with the simulation obtained considering a perpendicular or a diagonal orientation of the sensors under test to the core reactor centre, respectively, as reported in Tables 2 and 3. The 12% uncertainty on the  $c$  factor is not added to the data points, as the comparison between data and simulation concentrates on the trend of the fluence faced by the measured pads according to their position in the container volume and because of the strong correlation between the source of the uncertainty on  $c$  and the conversion of  $V_{GL}$  ratios into fluence.

The data results exhibit good agreement with the perpendicular orientation simulation both in the absolute value and in the observed

trend of the fluence variation inside the tested region of the F19 irradiation channel.

As mentioned above, in the simulation, the active part of each sensor is divided into  $5 \times 5$  sections, corresponding to the positions of individual pixels (see Fig. 1), and fast neutron flux is calculated for each pixel. Fig. 17 compares measured fluences from data and perpendicularly oriented simulation averaged over rows of each column in every sensor. As can be seen, the agreement is good and exhibits a very high sensitivity of measured  $V_{GL}$  to the received fast neutron fluence. It is worth noting that the variations of the neutron flux inside the reactor core can be sensed with a millimetre spatial resolution.

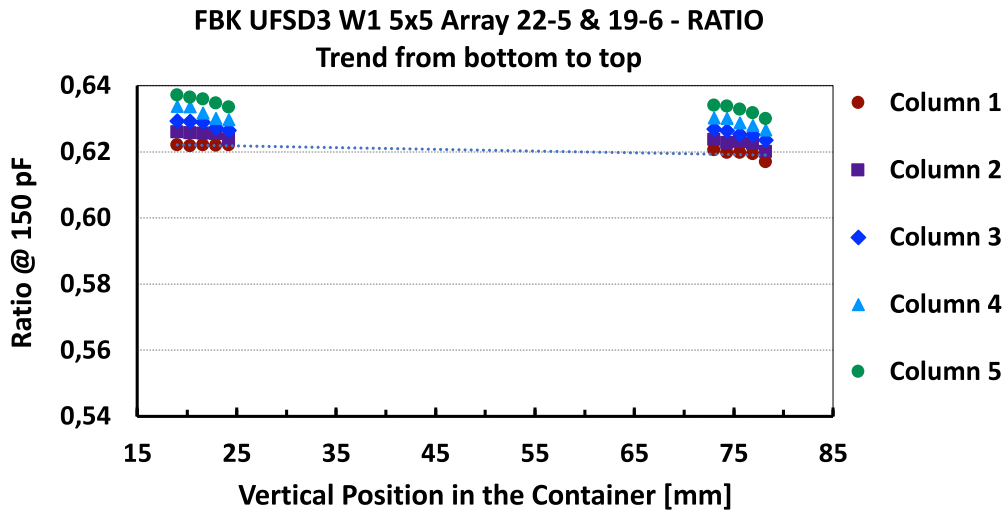


Fig. 13. The ratio of the  $V_{GL}$  values before and after irradiation two sensors placed on the same arm of the plastic structure.

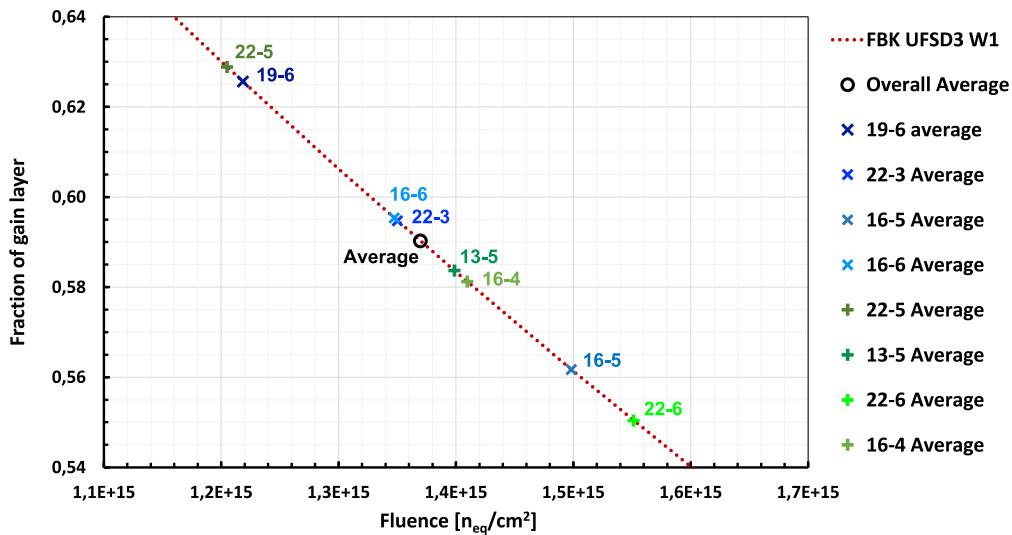


Fig. 14. Average fluence seen by the eight sensors under test. The overall average is also shown (black circle).

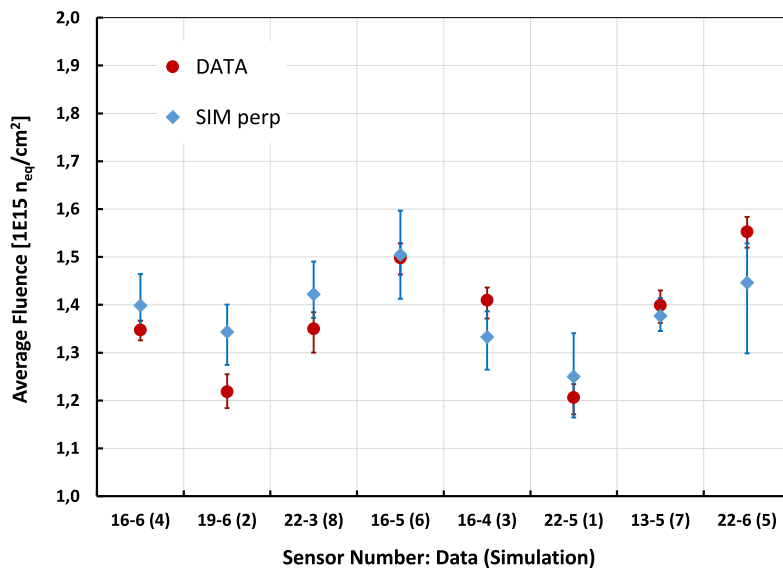


Fig. 15. Comparison of the average fluence measured by the sensors and the simulated fluence for sensors oriented perpendicularly to the reactor core centre. Error bars represent the minimum and maximum fluence measured by the pixels in each sensor. The error on the  $c$  factor is not added to the data. Reactor power has been set to 250kW for 926 s.



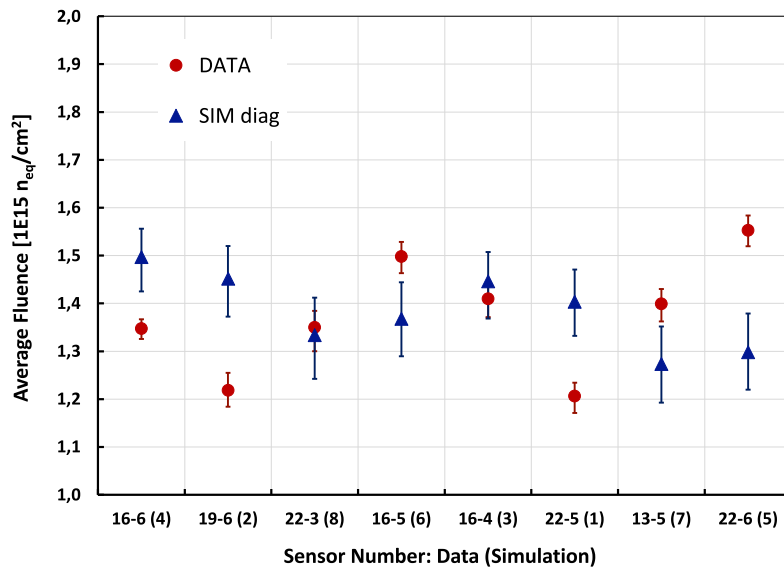


Fig. 16. Comparison of the average fluence measured by the sensors and the simulated fluence for sensors oriented diagonally to the reactor core centre. Error bars represent the minimum and maximum fluence measured by the pixels in each sensor. The error on the  $c$  factor is not reported on the data. Reactor power has been set to 250 kW for 926 s.

## 7. Conclusions

The fluence profile on channel F19 at the JSI TRIGA reactor has been measured with LGAD sensors made by an array of  $5 \times 5$  pixel with  $1.3 \text{ mm} \times 1.3 \text{ mm}$  area. Eight different LGAD sensors taken from the same wafer from the UFSD3 production batch of the FBK foundry have been tested: sensors have been fixed on cross-shaped plastic support at two different depths and inserted on the plastic container used for the irradiation.

The bias at which the gain implant is depleted,  $V_{GL}$ , has been extracted from C-V measurements for each pixel of the tested sensors, before and after the irradiation to  $1.5 \times 10^{15} \text{ n}_{eq}/\text{cm}^2$ . From the ratio of the  $V_{GL}$  values before and after irradiation, the fluence experienced by every pixel has been extracted.

An average fluence of  $1.37 \times 10^{15} \text{ n}_{eq}/\text{cm}^2$  has been measured, 8.7% lower than the nominal value. A spread in the delivered fluence inside the tested channel has been observed: the difference in fluence around the central value has been quantified between -14.7% to 15.4%. The flux of neutrons on the tested region of the reactor core has been simulated using MCNP v.6.1 code with ENDF/B-VII.0 nuclear data libraries and confirms the experimental observations.

The position of the container inside the F19 channel, together with the orientation of the sensor, is unknown. But the experimental results are in good agreement with the simulation of a perpendicular orientation of the sensors to the reactor core.

Only a minor vertical variation of the fluence has been observed, in agreement with the simulation, with a maximum observed spread of  $7.81 \times 10^{13} \text{ n}_{eq}/\text{cm}^2$  from the top to the bottom of the tested volume.

The presented study proves a very high sensitivity of the  $V_{GL}$  ratio technique for measurements of neutron flux, and its validity is well confirmed by the good agreement with the simulation. The fine granularity of the LGAD devices and the relatively simple measurement approach offers the possibility of monitoring neutron flux uniformity with millimetre spatial resolution. LGAD sensors demonstrated their effectiveness as precise monitors of the neutron flux inside a reactor core.

### CRedit authorship contribution statement

**V. Sola:** Conceptualization, Data curation, Formal analysis, Investigation, Methodology, Project administration, Validation, Visualization,

Writing – original draft, Writing – review & editing. **I. Mandić:** Conceptualization, Data curation, Formal analysis, Investigation, Methodology, Writing – original draft, Writing – review & editing, Validation, Visualization. **K. Ambrožič:** Conceptualization, Formal analysis, Methodology, Software, Visualization, Writing – original draft, Writing – review & editing. **O.A. Marti Villarreal:** Data curation. **M. Ferrero:** Conceptualization, Data curation, Formal analysis, Investigation, Methodology. **G. Kramberger:** Formal analysis, Resources, Supervision. **L. Snoj:** Project administration, Resources, Supervision.

### Declaration of competing interest

The authors declare that they have no known competing financial interests or personal relationships that could have appeared to influence the work reported in this paper.

### Data availability

Data will be made available on request.

### Acknowledgements

The authors acknowledge Nicolò Cartiglia, Roberta Arcidiacono and the whole UFSD Torino group for providing the LGAD sensors used for the analysis and for the continuous and fruitful discussion and support. The authors thank Gian Franco Dalla Betta, Lucio Pancheri, Maurizio Boscardin, Giovanni Paternoster and the FBK SD group for designing and producing the tested sensors. The authors thank the RD50 Collaboration (CERN) for providing suggestions and discussion that triggered the presented study. The authors acknowledge the financial support from the Slovenian Research Agency (research core funding no. P1-0135 and project no. J1-6199). The authors acknowledge the financial support from the INFN CSN5 through the eXFlu research project and the FRIDA call. The authors acknowledge the financial support from the Fondazione Compagnia di San Paolo.

### Appendix. Sensor assembly modelled isotopic composition and densities

See Tables A.4–A.6.

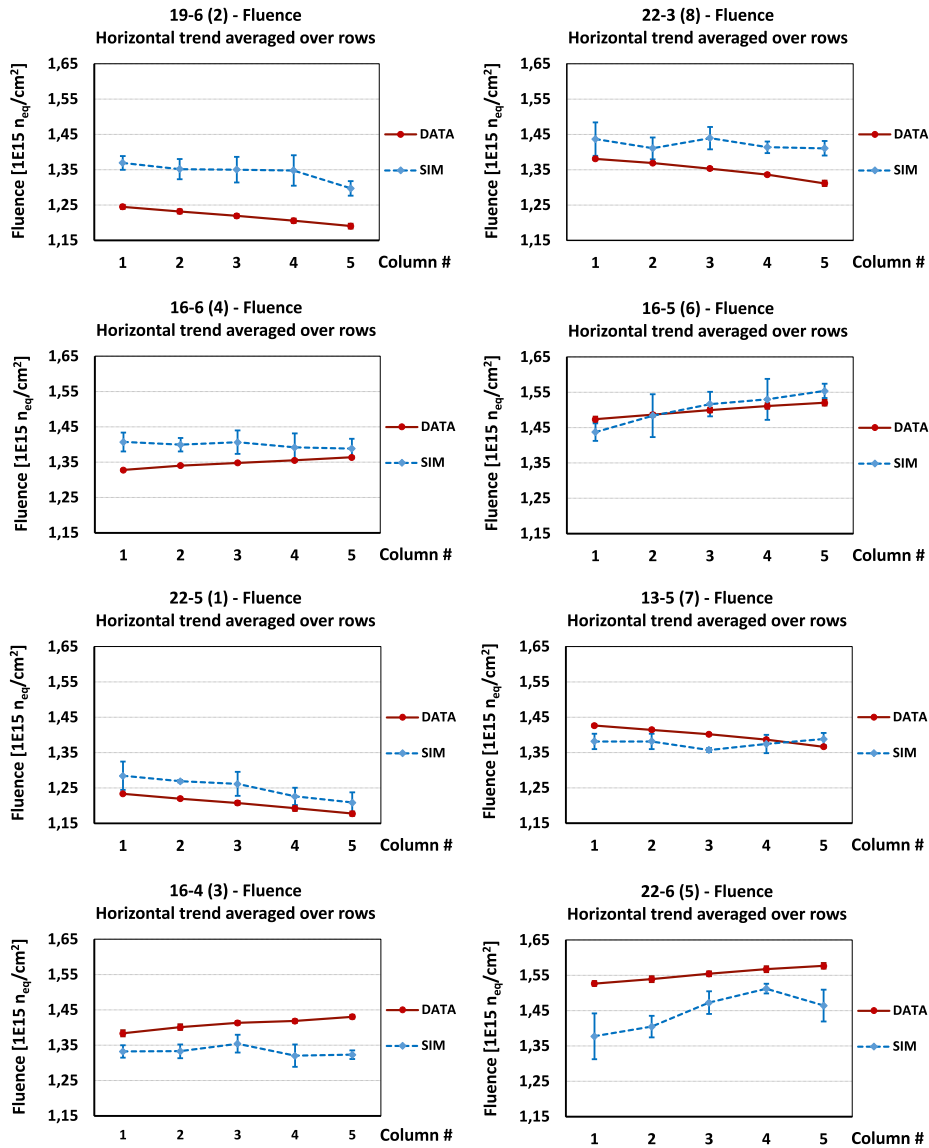


Fig. 17. Comparison of the fluence values as measured by the devices and simulated assuming a perpendicular orientation with respect to the reactor core centre. Single plots refer to single measured (simulated) 5 × 5 sensors. The fluences are shown as a function of the column number, averaged over the 5 rows belonging to the same column, and error bars indicate the standard deviation of the fluence values from pixels in the same column.

Table A.4

Isotopic composition of the sensor modelled in pure silicon, with density of  $\rho = 2.33 \text{ g cm}^{-3}$ .

Isotope	Number density [ $\times 10^{24} \text{ cm}^{-3}$ ]
$^{28}\text{Si}$	$4.6075 \times 10^{-2}$
$^{29}\text{Si}$	$2.3406 \times 10^{-3}$
$^{30}\text{Si}$	$1.5448 \times 10^{-3}$

Table A.5

Isotopic composition of the capton tape, with density of  $\rho = 1.42 \text{ g cm}^{-3}$ .

Isotope	Number density [ $\times 10^{24} \text{ cm}^{-3}$ ]
$^1\text{H}$	$5.1250 \times 10^{-2}$
$^{nat}\text{C}$	$5.1248 \times 10^{-2}$
$^{14}\text{N}$	$8.5102 \times 10^{-3}$
$^{15}\text{N}$	$3.1090 \times 10^{-5}$
$^{16}\text{O}$	$4.2705 \times 10^{-3}$

Table A.6

Isotopic composition of the FR4 board holder, with density of  $\rho = 1.85 \text{ g cm}^{-3}$ .

Isotope	Number density [ $\times 10^{24} \text{ cm}^{-3}$ ]
$^{10}\text{B}$	$6.3686 \times 10^{-4}$
$^{11}\text{B}$	$2.5634 \times 10^{-3}$
$^{16}\text{O}$	$3.4641 \times 10^{-2}$
$^{24}\text{Mg}$	$2.4018 \times 10^{-3}$
$^{25}\text{Mg}$	$3.0406 \times 10^{-4}$
$^{26}\text{Mg}$	$3.3477 \times 10^{-4}$
$^{27}\text{Al}$	$3.0595 \times 10^{-3}$
$^{28}\text{Si}$	$9.2342 \times 10^{-3}$
$^{29}\text{Si}$	$4.6910 \times 10^{-4}$
$^{30}\text{Si}$	$3.0960 \times 10^{-4}$
$^{40}\text{Ca}$	$2.1185 \times 10^{-3}$
$^{42}\text{Ca}$	$1.4139 \times 10^{-5}$
$^{43}\text{Ca}$	$2.9503 \times 10^{-6}$
$^{44}\text{Ca}$	$4.5587 \times 10^{-5}$
$^{46}\text{Ca}$	$8.7416 \times 10^{-8}$
$^{48}\text{Ca}$	$4.0867 \times 10^{-6}$

## References

- [1] A. Kolšek, et al., Using TRIGA mark II research reactor for irradiation with thermal neutrons, *Nucl. Eng. Des.* 283 (2015) 155–161, <http://dx.doi.org/10.1016/j.nucengdes.2014.03.012>.
- [2] RD50 Collaboration, M. Moll, et al., RD50 Status Report 2009/2010 – Radiation Hard Semiconductor Devices for Very High Luminosity Colliders, CERN-LHCC-2012-010, LHCC-SR-004, 2012.
- [3] S. Mazza, et al., Beam test studies of the LGAD sensors at FNAL, in: TREDI2020 – 15<sup>th</sup> Trento Workshop on Advanced Silicon Radiation Detectors, TU Wien, Austria, 2020, URL <https://indico.cern.ch/event/813597/contributions/3727776>.
- [4] G. Pellegrini, et al., Technology developments and first measurements of low gain avalanche detectors (LGAD) for high energy physics applications, *Nucl. Instrum. Methods A* 765 (2014) 12–16, <http://dx.doi.org/10.1016/j.nima.2014.06.008>.
- [5] G. Kramberger, et al., Radiation effects in low gain avalanche detectors after hadron irradiations, *J. Instrum.* 10 (2015) P07006, <http://dx.doi.org/10.1088/1748-0221/10/07/P07006>.
- [6] M. Ferrero, et al., Radiation resistant LGAD design, *Nucl. Instrum. Methods A* 919 (2019) 16–26, <http://dx.doi.org/10.1016/j.nima.2018.11.121>.
- [7] M. Tornago, et al., Performances of the third UFSO production at FBK, in: 33<sup>th</sup> RD50 Workshop, CERN, Switzerland, 2018, URL <https://indico.cern.ch/event/754063/contributions/3222642>.
- [8] M. Ferrero, et al., A summary of the radiation resistance of carbonated gain implants, in: TREDI2021 – 16<sup>th</sup> Trento Workshop on Advanced Silicon Radiation Detectors, Virtual, 2021, URL <https://indico.cern.ch/event/983068/contributions/4223173/>.
- [9] M. Ferrero, et al., Recent studies and characterization on UFSO sensors, in: 34<sup>th</sup> RD50 Workshop, Lancaster, United Kingdom, 2019, URL <https://indico.cern.ch/event/812761/contributions/3459068/>.
- [10] L. Snoj, G. Žerovnik, A. Trov, Computational analysis of irradiation facilities at the JSI TRIGA reactor, *Appl. Radiat. Isot.* 70 (2012) 483–488, <http://dx.doi.org/10.1016/j.apradiso.2011.11.042>.
- [11] J.T. Goorley, et al., Initial MCNP6 release overview – MCNP6 version 1.0, 2013, <http://dx.doi.org/10.2172/1086758>.
- [12] M.B. Chadwick, et al., ENDF/B-VII.0: next generation evaluated nuclear data library for nuclear science and technology, *Nucl. Data Sheets* 107 (2006) 2931–3060, <http://dx.doi.org/10.1016/j.nds.2006.11.001>.
- [13] G. Žerovnik, M. Podvratnik, L. Snoj, On normalization of fluxes and reaction rates in MCNP criticality calculations, *Ann. Nucl. Energy* 63 (2014) 126–128, <http://dx.doi.org/10.1016/j.anucene.2013.07.045>.
- [14] A. Trkov, et al., On the self-shielding factors in neutron activation analysis, *Nucl. Instrum. Methods A* 610 (2009) 553–565, <http://dx.doi.org/10.1016/j.nima.2009.08.079>.
- [15] M. Ferrero, R. Arcidiacono, M. Mandurrino, V. Sola, N. Cartiglia, An Introduction to Ultra-Fast Silicon Detectors, CRC Press, 2021, <http://dx.doi.org/10.1201/9781003131946>.